

## Highlights

### **WaveGraphNet: Physics-Consistent Guided-Wave Damage Localization through Coupled Inverse-Forward Graph Learning**

Vinay Sharma, Aditya Bharade, Olga Fink

- Sparse guided-wave damage localization is formulated as a graph-based regression problem, mapping transducer-network observations to damage coordinates.
- A coupled inverse-forward graph architecture encourages consistent localization via path-wise energy-deviation patterns.
- Evaluation on the OGW-1 SHM Plate includes two spatially held-out train-test splits of increasing difficulty, assessing extrapolation to unseen damage zones.

# WaveGraphNet: Physics-Consistent Guided-Wave Damage Localization through Coupled Inverse–Forward Graph Learning

Vinay Sharma<sup>a,1</sup>, Aditya Bharade<sup>a,1</sup>, Olga Fink<sup>a,\*</sup>

<sup>a</sup>*EPFL, Intelligent Maintenance and Operations Systems, Lausanne, Switzerland*

---

## Abstract

Guided-wave structural health monitoring enables damage localization in composite plates using sparse networks of bonded piezoelectric transducers. However, inferring the spatial location of defects from pitch-catch measurements remains weakly constrained when only a limited set of damage locations is available for training. As a result, models trained to predict defect locations may perform well on seen cases but generalize poorly to unseen regions of the structure.

This paper proposes *WaveGraphNet*, a coupled inverse–forward graph learning framework for guided-wave damage localization in Carbon Fiber Reinforced Polymer (CFRP) plates. The sensing layout is explicitly modeled as a graph, where transducers are represented as nodes and measured propagation paths define the graph connectivity. An inverse branch maps graph-structured spectral descriptors of differential guided-wave responses to a damage location, while a forward branch predicts the path-wise energy-deviation patterns of measured wave responses associated with a candidate location. During training, the forward branch serves as a physics-consistent regularizer, discouraging location estimates that are numerically plausible but inconsistent with the measured redistribution of wave-response energy. This coupling encourages agreement between inferred damage coordinates and the underlying wave propagation behavior.

Within this benchmark, the proposed graph-based formulation provides a strong localization model for sparse guided-wave sensing and demonstrates

---

\*Corresponding author

<sup>1</sup>These authors contributed equally to this work.

improved robustness in extrapolation to held-out regions compared to both non-graph and graph baselines. These results highlight the potential of coupled inverse-forward graph learning as an effective strategy for guided-wave localization under limited spatial coverage.

*Keywords:* Guided-wave structural health monitoring, graph neural networks, damage localization, spatial generalization, composite plates

---

## 1. Introduction

Engineering structures require monitoring strategies that can detect and localize barely visible or internal damage before it propagates to a critical state [1]. Composite materials, and in particular Carbon Fiber Reinforced Polymers (CFRP), present unique challenges in this context due to their anisotropy and complex damage mechanisms. For structural health monitoring (SHM) to be practically useful, however, methods must bridge the persistent gap between controlled laboratory demonstrations and reliable field deployment [2]. Guided ultrasonic waves are attractive in this context because they can interrogate relatively large plate-like regions using sparse networks of surface-bonded piezoelectric transducers [3, 4, 5]. Such sensing layouts are especially relevant for composite structures, including CFRP components, and recent reviews emphasize the broader importance of guided waves for SHM and long-range nondestructive testing [6, 7]. The central challenge, however, is that damage location is never observed directly; it must be inferred from how a defect perturbs multiple actuator-receiver paths across a sparse sensing network.

This inverse mapping is difficult even under controlled experimental conditions. Composite anisotropy, multimodal propagation, dispersion, boundary reflections, and limited path coverage all reduce identifiability, especially when different damage locations produce similar scattered responses [3, 5]. The problem becomes more severe when only a small number of labeled damage positions is available for model development, which is the realistic regime for many SHM applications. A localization model may therefore appear accurate on the sampled damage grid while remaining unreliable in unsampled regions of the structure, where it must effectively extrapolate beyond the locations seen during training. In SHM, this is not merely an evaluation detail but a deployment issue: practical systems must remain reliable beyond the specific defect locations observed during data collection [2].

Recent machine learning approaches have improved guided-wave damage assessment by learning damage-sensitive representations directly from measured signals. Reviews of the guided-wave literature highlight both the promise of such methods and the difficulty of training them from limited labeled experiments [8]. In particular, several approaches transform the measured signals into alternative representations and apply neural networks for localization. For example, Gramian-angular-field encodings combined with convolutional networks have been used for localization from transformed guided-wave signals [9]. Other works rely on engineered signal features, and neural models have also been developed for joint localization and severity assessment in laminated composites [10, 11]. In addition, unified pipelines for detection, localization, and quantification have been proposed [12]. Despite their success, these approaches share a common limitation: they treat the measurements as arrays, sequences, or images, without explicitly accounting for the underlying sensing topology. Consequently, they do not fully exploit the relational structure induced by the transducer network, where each measurement corresponds to a specific actuator–receiver path with well-defined geometric and physical meaning.

In sparse guided-wave SHM, damage localization must be inferred from a limited set of actuator-receiver measurements distributed across the structure. Each propagation path provides only a partial observation of the defect through changes in the transmitted wavefield, and the informativeness of this response depends strongly on the path geometry, propagation direction, and relative position of the defect. As a result, no single path is sufficient for reliable localization; the defect location must instead be inferred by integrating weak and spatially distributed evidence across multiple transducer pairs.

This makes the problem inherently relational. A natural representation is therefore a graph, where transducers are modeled as nodes and actuator-receiver paths as edges carrying both the measured responses and associated geometric information. Such a formulation allows the model to learn how information should be aggregated across paths, rather than treating each signal independently.

Graph neural networks provide a principled framework for this setting. Message passing enables learning from node-edge interactions [13, 14], while graph convolution and attention introduce mechanisms to weight heterogeneous neighborhood information [15, 16]. Related physics-informed graph models further illustrate the usefulness of interaction-based inductive biases in industrial systems [17]. In structural health monitoring and related sens-

ing problems, these approaches are increasingly adopted when the sensing topology itself provides a meaningful inductive bias [18, 19].

However, incorporating graph structure alone does not resolve the central ambiguity of sparse localization. Under limited sensing coverage, multiple defect locations may remain consistent with similar patterns of path-wise response, particularly when localization is formulated as a supervised direct coordinate regression problem trained on a finite set of labeled damage locations. In such cases, a model may predict a numerically plausible coordinate while failing to preserve consistency with the measured redistribution of guided-wave response across the network.

Guided-wave graph models for damage detection and localization have already demonstrated the benefits of representing the sensing network explicitly, including graph-in-graph formulations for ultrasonic guided waves and physics-augmented spatio-temporal graph networks [20, 21]. These approaches leverage relational structure to improve feature extraction and prediction, but typically treat localization as a direct mapping from measurements to outputs, and therefore do not resolve the ambiguity inherent to sparse coordinate regression, particularly under spatial extrapolation beyond the training domain.

Similarly, physics-guided guided-wave methods have shown that incorporating propagation knowledge can improve predictive performance [22, 23]. However, such approaches generally introduce physics through model-assisted supervision, simulated augmentation, or signal enhancement, rather than enforcing that predicted coordinates remain consistent with the observed redistribution of path-wise response. While related ideas of consistency-based regularization have been explored in inverse problems, they are predominantly developed in imaging and partial differential equations (PDE)-contexts [24, 25], rather than in sparse transducer-network localization settings.

The key gap, therefore, is the absence of a framework that combines sparse graph-based coordinate regression with an explicit consistency mechanism ensuring that predicted damage locations remain compatible with the measured guided-wave response, particularly under spatial extrapolation.

To address this limitation, we propose *WaveGraphNet*, an inverse-forward graph framework for sparse guided-wave damage localization. The inverse branch estimates defect coordinates from graph-structured measurements, while the forward branch predicts the path-wise redistribution of wave-response energy induced by a candidate defect location. During training, the forward

prediction acts as a consistency constraint on the inverse estimate, encouraging predicted coordinates to remain compatible with the measured response pattern across the sensing network. The model is therefore designed not only to regress damage coordinates, but also to encourage agreement between the predicted locations and the spatial distribution of guided-wave evidence.

The main contributions of this work are as follows:

- We formulate sparse guided-wave damage localization as a graph-to-coordinate regression problem that explicitly represents transducers as nodes and propagation paths as edges.
- We propose *WaveGraphNet*, a coupled inverse–forward graph framework in which coordinate prediction is regularized by a learned forward model of path-wise energy deviation.
- We adopt a unified regression setting that embeds pristine and damaged states in the same output space through a designated no-damage target.
- We evaluate the framework on the Open Guided Wave (OGW)-1 SHM Plate benchmark using two spatially held-out train–test splits of increasing difficulty, designed to probe localization in unseen damage zones rather than interpolation on an observed damage grid.

The remainder of the paper is organized as follows. Section 2 positions the work with respect to guided-wave localization, graph-based SHM, and physically guided inverse learning. Section 3 defines the localization problem and the consistency signal used for regularization. Section 4 presents the proposed *WaveGraphNet* architecture and training strategy. Section 5 describes the OGW-1 SHM Plate case study and evaluation protocol. Sections 6 and 7 present the benchmark design and localization results. Section 8 concludes the paper.

## 2. Related Work

This work relates to three areas: learning-based guided-wave localization, graph-based modeling for SHM, and physically guided learning for inverse problems.

**Learning-based guided-wave localization** approaches have demonstrated that damage-sensitive information can be extracted directly from measured guided-wave signals. Existing methods typically represent the

data as time-series arrays, engineered feature vectors, or image-like transformations. For example, Gramian-angular-field representations combined with convolutional neural networks have been used for damage localization [9]. Feature-based neural models using engineered envelope characteristics of scattered Lamb-wave signals have also been proposed for damage localization in composite structures [10], while deep learning models operating directly on raw Lamb-wave signals have addressed joint localization and severity assessment [11]; unified deep learning frameworks have also addressed detection, localization, and quantification within a single framework [12]. These studies demonstrate that learned representations can capture informative damage signatures. However, they generally process measurements as arrays, sequences, or images, and thus formulate the problem primarily at the signal level, without explicitly modeling the relational structure induced by the transducer network.

**Graph-based modeling** is particularly relevant for SHM, as sensor layout, structural connectivity, and spatial dependencies play a central role in structural damage inference [18, 19]. Recent work has leveraged graph-based models for damage detection and localization in aerospace and sensor-network-based SHM settings [26]. In guided-wave monitoring more specifically, graph neural networks have been used to represent sparse transducer interactions for damage detection and localization [20, 21]. This direction is well motivated: localization depends on the joint perturbation pattern across multiple propagation paths, and graph neural networks provide a principled framework for learning from node–edge interactions through message passing, graph convolutions, and attention mechanisms [13, 14, 15, 16]. However, existing graph-based guided-wave approaches typically treat localization as a direct prediction problem and have not explicitly addressed sparse guided-wave *coordinate* regression under spatial hold-out conditions, where test defects lie in regions not represented during training.

**Physically guided approaches** provide a complementary perspective by incorporating prior knowledge of wave propagation. In guided-wave SHM, learning-based approaches have combined measured data with simulated guided wave responses generated by reduced-order spectral finite-element forward models [22], and physics-guided methods have been used to suppress boundary-reflection effects by enforcing time-of-flight consistency for damage-scattered Lamb waves prior to downstream inference [23]. More broadly, the inverse-problem literature has shown that forward consistency, learned regularization, and physics-informed supervision can reduce ambigu-

ity when direct inversion is weakly constrained [24, 25, 27, 28]. These insights are particularly relevant to sparse guided-wave localization, where limited path coverage and sparse spatial supervision can render coordinate regression underdetermined. However, existing guided-wave approaches typically incorporate physics through supervision, data augmentation, or preprocessing, rather than using a learned forward surrogate to explicitly enforce that predicted damage locations remain consistent with the observed redistribution of path-wise responses, especially under spatial extrapolation.

Existing work therefore highlights three complementary strengths: learning-based methods can extract damage-sensitive features from measured signals, graph-based approaches can encode the relational structure induced by the sensing topology, and physics-guided methods can reduce ambiguity through additional constraints. What remains insufficiently addressed is the integration of these elements for sparse guided-wave *coordinate* localization in spatially unseen regions. In particular, current approaches lack a mechanism to enforce consistency between predicted damage locations and the measured redistribution of guided-wave response across the transducer network.

In this work, we address this setting by coupling an inverse graph-based localizer with a learned forward model of path-wise energy deviation. The forward model acts as a consistency constraint during training, encouraging predicted coordinates to remain compatible with the observed response pattern across the sensing network. We further evaluate the proposed framework under a train–test protocol that withholds entire damage regions during training, thereby explicitly assessing its ability to generalize beyond the spatial support of the training data.

### 3. Problem Formulation

We consider a guided-wave SHM system with  $N$  piezoelectric transducers bonded to a composite plate and operated in pitch–catch mode. Each transducer can act either as an actuator or as a receiver. Let  $V = \{1, \dots, N\}$  denote the transducer set, and let  $\mathbf{r}_i \in \mathbb{R}^2$  be the in-plane coordinate of transducer  $i$ .

The acquisition provides a set of measured pitch–catch channels, denoted by  $\mathcal{P}$ . Each element of  $\mathcal{P}$  corresponds to one measured actuator–receiver transmission between two distinct transducers. We refer to each such measured channel as a *propagation path*. Along this channel, the emitted guided

wave travels through the plate, interacts with the structure, and may be perturbed by damage before being recorded at the receiver.

In the OGW-1 acquisition protocol, one measurement is available for each unordered transducer pair. Therefore, reciprocal measurements  $(i, j)$  and  $(j, i)$  are not treated as distinct measured channels. For  $N = 12$ , this gives

$$|\mathcal{P}| = \binom{12}{2} = 66 \quad (1)$$

measured propagation paths per sample. For notational convenience, we write a measured path as  $(i, j) \in \mathcal{P}$ , where  $i$  denotes the actuator and  $j$  the receiver in the recorded acquisition. However, this notation does not imply that the reciprocal measurement  $(j, i)$  is also available. If both reciprocal actuator–receiver directions were acquired, the corresponding bi-directional acquisition would contain  $N(N - 1)$  channels.

The inverse and forward branches use the measured path set differently. The inverse branch uses all measured propagation paths in  $\mathcal{P}$ . In the graph implementation, each measured transducer pair is represented using bi-directional message-passing edges, yielding  $2|\mathcal{P}|$  graph edges. The two message-passing directions share the same features derived from the measured signal on the corresponding paths.

The forward consistency branch uses a selected subset  $\mathcal{P}_f \subset \mathcal{P}$ . This subset contains the plate-spanning propagation paths connecting the two opposite boundary rows of transducers. This subset selection is inspired by prior work on the OGW benchmark, where the 36 paths connecting the upper and lower transducer arrays were retained for damage localization [29]. Let  $V_{\text{top}}$  and  $V_{\text{bottom}}$  denote the top and bottom transducer rows, respectively. Then

$$\mathcal{P}_f = \{(i, j) \in \mathcal{P} : \{i, j\} \cap V_{\text{top}} \neq \emptyset, \{i, j\} \cap V_{\text{bottom}} \neq \emptyset\}. \quad (2)$$

For the OGW-1 plate,  $|V_{\text{top}}| = |V_{\text{bottom}}| = 6$ , and hence

$$|\mathcal{P}_f| = 6 \times 6 = 36. \quad (3)$$

These paths are selected for the forward consistency target because they connect opposite sides of the plate and traverse the monitored interior, making their energy variations a compact summary of damage-induced redistribution across the sensing network. The remaining measured paths are still used by

the inverse branch, but they are not included in the forward energy-deviation target.

For each measured propagation path  $(i, j) \in \mathcal{P}$ , a discrete response

$$s_{ij}(t), \quad t = 1, \dots, T, \quad (4)$$

is recorded over  $T$  time samples. The objective is to infer the in-plane coordinate of a single defect,

$$\mathbf{p} = [x_d, y_d]^\top \in \Omega \subset \mathbb{R}^2, \quad (5)$$

from the collection of path-wise guided-wave responses. Beyond accurate localization at sampled defect positions, we explicitly target robustness under spatial extrapolation, where  $\mathbf{p}$  lies in regions not represented during training.

### 3.1. Damage-sensitive signal representation

The raw signals contain strong direct arrivals, boundary reflections, and measurement noise, which can obscure defect-induced effects. To isolate damage-sensitive perturbations, a pristine reference is estimated for each propagation path and subtracted from the measured response. Let  $\bar{s}_{ij}(t)$  denote the mean healthy-state signal for path  $(i, j)$ . The differential signal is defined as

$$\delta s_{ij}(t) = s_{ij}(t) - \bar{s}_{ij}(t). \quad (6)$$

This baseline subtraction is standard in guided-wave interrogation, as it suppresses the dominant healthy contribution while retaining the residual associated with damage [30, 31].

Each differential signal is then transformed into the frequency domain over a selected band  $\mathcal{F} = \{f_1, \dots, f_K\}$ . For each path  $(i, j)$  and frequency bin  $f_k$ , we extract amplitude and phase from the Fourier transform of  $\delta s_{ij}$ :

$$A_{ij}(f_k) = |\mathcal{F}\{\delta s_{ij}\}(f_k)|, \quad \phi_{ij}(f_k) = \angle \mathcal{F}\{\delta s_{ij}\}(f_k), \quad (7)$$

These quantities are assembled into a path-wise descriptor

$$\mathbf{z}_{ij} = \left[ \tilde{A}_{ij}(f_1), \dots, \tilde{A}_{ij}(f_K), \phi_{ij}(f_1), \dots, \phi_{ij}(f_K) \right]^\top \in \mathbb{R}^{2K}. \quad (8)$$

Here  $\tilde{A}_{ij}(f_k)$  denotes amplitude normalized using statistics computed exclusively on the training partition. The frequency band and the descriptor

dimensionality are fixed across all models to ensure that performance differences arise from model design rather than variations in input representation. This formulation provides a compact yet informative encoding of path-wise scattering behavior, suitable for learning under limited data while preserving features relevant to defect localization.

### 3.2. Graph representation of one measurement sample

Damage localization depends on how a defect jointly perturbs multiple measured propagation paths. To capture this relational structure, each measurement sample is represented using graph-structured observations over the transducer set  $V$ . The graph connectivity is induced by the measured path set  $\mathcal{P}$ , where each measured propagation path corresponds to one available pitch-catch channel between two distinct transducers.

For the inverse branch, we define the measured-response graph as

$$\mathcal{G}_{\text{inv}} = (V, E_{\text{inv}}). \quad (9)$$

Here, the nodes correspond to transducers, and the edge set  $E_{\text{inv}}$  contains the bi-directional message-passing edges associated with all measured propagation paths in  $\mathcal{P}$ . Thus, each measured path contributes two graph edges for message passing, while both directions share the same measured spectral descriptor extracted from the corresponding guided-wave response. This representation allows information from all path-wise measurements to be aggregated across the sensing network.

For the forward consistency branch, we use a separate graph that shares the same node set as the inverse graph, while its connectivity is restricted to the selected propagation-path subset  $\mathcal{P}_f \subset \mathcal{P}$ , defined in Section 3. This graph is written as

$$\mathcal{G}_{\text{fwd}} = (V, E_{\text{fwd}}), \quad (10)$$

where  $E_{\text{fwd}}$  contains the bi-directional message-passing edges associated only with the selected paths in  $\mathcal{P}_f$ . Consequently, the inverse branch operates on all measured propagation paths, whereas the forward branch is restricted to the plate-spanning paths used to define the forward consistency target.

The branch-specific edge features are defined in Section 4. In brief, the inverse graph uses measured spectral descriptors of the guided-wave responses, whereas the forward graph uses defect-conditioned geometric features relative to a candidate damage location. The inverse localization problem is then

formulated as

$$\hat{\mathbf{p}} = f(\mathcal{G}_{\text{inv}}), \quad (11)$$

where  $f(\cdot)$  maps the measured-response graph to a predicted defect coordinate.

### 3.3. Limitations of coordinate-only regression

Equation (11) is inherently weakly constrained under sparse sensing configurations. In such settings, distinct defect locations can induce similar perturbations across overlapping sets of propagation paths, particularly when the training data covers only a limited subset of the admissible domain. As a result, a model trained solely to minimize coordinate error may interpolate well over the observed damage locations while producing predictions that are inconsistent with the underlying wave propagation in unseen regions. In other words, low regression error on the sampled locations does not guarantee that the inferred coordinate is physically plausible with respect to the measured redistribution of wave energy across the sensing network.

### 3.4. Energy deviation as the forward consistency target

To introduce an additional physical constraint, we summarize the effect of damage on each propagation path by a scalar energy-deviation quantity  $\Delta E_{ij}$ . This quantity captures how the presence of a defect redistributes spectral energy along a given path relative to the pristine state. In this study,  $\Delta E_{ij}$  is defined as the mean normalized amplitude deviation between the damaged and pristine responses over the frequency bins used in  $\mathbf{z}_{ij}$ . Let  $\tilde{A}_{ij}(f_k)$  denote the absolute normalized spectral amplitude of the differential signal for path  $(i, j)$  at frequency  $f_k$ , and let  $\bar{A}_{ij}(f_k)$  be the corresponding mean absolute normalized amplitude observed over pristine training samples. We define

$$\Delta E_{ij} = \frac{1}{E_{\text{max}}} \max \left( \frac{1}{K} \sum_{k=1}^K \left( \tilde{A}_{ij}(f_k) - \bar{A}_{ij}(f_k) \right), 0 \right), \quad (12)$$

where  $E_{\text{max}}$  is the maximum deviation observed over all training samples and selected forward-branch paths  $(i, j) \in \mathcal{P}_f$ . The non-negativity clamp retains only positive mean amplitude deviations relative to the pristine reference, while normalization by  $E_{\text{max}}$  maps the targets to  $[0, 1]$ . This equation gives one scalar value per propagation path.

Collecting these values over all propagation paths used by the forward model yields the path-wise energy-deviation vector

$$\Delta \mathbf{E} = [\Delta E_{ij}]_{(i,j) \in \mathcal{P}_f}, \quad (13)$$

where  $\mathcal{P}_f$  denotes the set of paths considered by the forward branch. The vector  $\Delta \mathbf{E}$  therefore contains one entry per selected measured propagation path and serves as the supervision target for the forward model.

This quantity defines an auxiliary consistency constraint. In particular, a predicted defect coordinate is considered physically consistent only if it induces a path-wise energy-deviation pattern that is compatible with the measured one.

The learning objective is therefore coupled. Given the measured-response graph  $\mathcal{G}_{\text{inv}}$ , the model should infer  $\hat{\mathbf{p}}$  such that

$$\hat{\mathbf{p}} \approx \mathbf{p}, \quad (14)$$

$$g(\hat{\mathbf{p}}; \mathcal{P}_f) \approx \Delta \mathbf{E}, \quad (15)$$

where  $g(\cdot)$  denotes the forward branch that maps a candidate defect location to the corresponding path-wise energy-deviation pattern over  $\mathcal{P}_f$ . The next section introduces the proposed framework, in which an inverse graph-based localizer is regularized by a forward model that predicts path-wise energy deviation, thereby encouraging consistency between inferred coordinates and measured wave responses.

#### 4. Proposed Framework

To address the ambiguity of coordinate-only regression introduced in Section 3, we design a framework that combines inverse prediction with an explicit forward consistency mechanism. The key idea is to ensure that predicted defect locations are not only close to the ground truth, but also consistent with the observed redistribution of guided-wave response across the sensing network. This is achieved by coupling a graph-based localizer with a learned forward model that evaluates whether a candidate coordinate induces a physically compatible path-wise response pattern.

The proposed *WaveGraphNet* architecture contains two coupled modules built on the same transducer layout but used for different purposes. The inverse module predicts the defect coordinate from measured guided-wave data,

whereas the forward module predicts the path-wise energy-deviation pattern associated with a candidate coordinate. The inverse graph is induced by all measured propagation paths in  $\mathcal{P}$  and encodes transducer coordinates, path geometry, and measured spectral descriptors. The forward graph is induced only by the selected path subset  $\mathcal{P}_f \subset \mathcal{P}$  and uses defect-conditioned geometric features to predict the path-wise energy-deviation target. The forward graph preserves the underlying transducer connectivity but redefines its edge features using geometric quantities relative to a defect location. Joint training encourages the inverse predictor to return coordinates that are not only close to the target but also compatible with the measured wave-response redistribution. Training is performed in three stages: inverse-branch pre-training with the localization loss, forward-branch pretraining using corresponding target coordinates, and final joint optimization with the coupled objective. Figure 1 summarizes the proposed *WaveGraphNet* architecture.

#### 4.1. Graph representation

The proposed framework uses two graph representations of the same sensing network. In both cases, the node set is identical, as it is determined by the transducer layout. The inverse graph is induced by all measured propagation paths in  $\mathcal{P}$ , whereas the forward graph is induced by the selected path subset  $\mathcal{P}_f \subset \mathcal{P}$  used to define the energy-deviation target. The inverse graph encodes measured path-wise spectral responses for localization, while the forward graph encodes geometry relative to a candidate defect location for consistency evaluation.

Each node  $i \in V$  represents a transducer and is associated with its spatial coordinate,

$$\mathbf{x}_i = \mathbf{r}_i. \quad (16)$$

For the inverse graph, each measured propagation path in  $\mathcal{P}$  is represented by bi-directional message-passing edges. Thus, the graph contains two message-passing directions for each measured path, while the measured spectral descriptor is shared by the two directions. For a message-passing edge from  $i$  to  $j$  associated with the measured propagation path between transducers  $i$  and  $j$ , the inverse edge feature is defined as

$$\mathbf{e}_{ij}^{\text{inv}} = [\mathbf{r}_j - \mathbf{r}_i, \|\mathbf{r}_j - \mathbf{r}_i\|_2, \mathbf{z}_{ij}]. \quad (17)$$

For the reciprocal message-passing direction, the geometric displacement is reversed, while the measured spectral descriptor is shared because only one

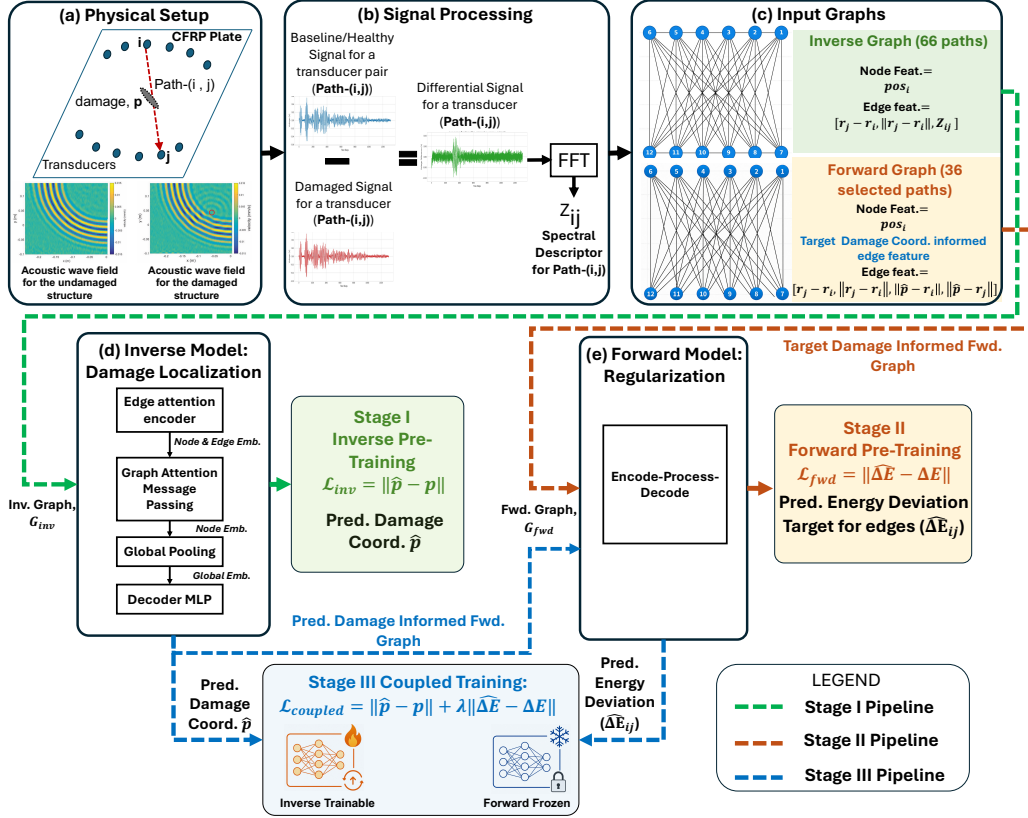


**Figure 1: Overview of the proposed *WaveGraphNet* framework.** (a) Guided-wave SHM setup for a CFRP plate with boundary-mounted transducers, where a defect at location  $\mathbf{p}$  perturbs the propagating wavefield. (b) Signal-processing pipeline in which the pristine response is subtracted from the measured signal and the resulting differential response is transformed to the frequency domain to obtain the path-wise spectral descriptor  $\mathbf{z}_{ij}$ . (c) Graph construction used by the two branches: the inverse graph  $G_{inv}$  is induced by all measured propagation paths, whereas the forward graph  $G_{fwd}$  uses the selected plate-spanning subset  $\mathcal{P}_f$ . (d) Inverse branch, which maps the measured-response graph to a predicted defect coordinate  $\hat{\mathbf{p}}$ . (e) Forward consistency branch, which maps a target- or predicted-coordinate-conditioned graph to the corresponding path-wise energy-deviation pattern  $\Delta\mathbf{E}$ . **Stage I:** the inverse branch is pretrained using the localization loss. **Stage II:** the forward branch is pretrained using the corresponding target coordinate. **Stage III:** the inverse branch is updated under forward-consistency regularization while the forward branch remains frozen.

measured channel is available for the corresponding transducer pair.

For the forward graph, each selected propagation path in  $\mathcal{P}_f$  is also represented by bi-directional message-passing edges and is reparameterized with respect to a candidate defect coordinate  $\hat{\mathbf{p}}$ . The corresponding edge feature vector is defined as

$$\mathbf{e}_{ij}^{\text{fwd}} = [\mathbf{r}_j - \mathbf{r}_i, \|\mathbf{r}_j - \mathbf{r}_i\|_2, \|\hat{\mathbf{p}} - \mathbf{r}_i\|_2, \|\hat{\mathbf{p}} - \mathbf{r}_j\|_2]. \quad (18)$$

Here, the first two terms describe the path geometry, while the latter two encode the relative position of the candidate defect with respect to the two end transducers of the path. For the reciprocal message-passing direction, the geometric displacement is reversed, and the two candidate-to-transducer distances are ordered according to the corresponding source and target nodes. This representation allows the forward model to map a hypothesized defect location to a predicted energy-deviation response over the selected propagation paths.

Accordingly, the inverse and forward graphs are given by

$$\mathcal{G}_{\text{inv}} = (V, E_{\text{inv}}, \{\mathbf{x}_i\}_{i \in V}, \{\mathbf{e}_{ij}^{\text{inv}}\}_{(i,j) \in E_{\text{inv}}}), \quad (19)$$

$$\mathcal{G}_{\text{fwd}}(\hat{\mathbf{p}}) = (V, E_{\text{fwd}}, \{\mathbf{x}_i\}_{i \in V}, \{\mathbf{e}_{ij}^{\text{fwd}}\}_{(i,j) \in E_{\text{fwd}}}). \quad (20)$$

Both graphs share the same node representation defined by the transducer layout but differ in their edge sets and edge feature definitions. Here,  $E_{\text{inv}}$  is induced by all measured paths in  $\mathcal{P}$ , whereas  $E_{\text{fwd}}$  is induced only by the selected paths in  $\mathcal{P}_f$ . In both cases, the graph edges denote message-passing directions induced by the measured propagation paths rather than additional measured channels.

#### 4.2. Inverse localization module

The inverse module is the primary predictor:

$$\hat{\mathbf{p}} = f_{\theta}(\mathcal{G}_{\text{inv}}). \quad (21)$$

Its objective is to map distributed path-wise scattering information to a single defect coordinate. Since not all measured propagation paths and frequency components contribute equally to localization, the model incorporates two levels of selectivity: an attention-based edge encoder that compresses spectral descriptors into latent representations, and attention-based message passing that emphasizes informative interactions across the sensing network.

**Table 1:** Summary of graph features used in the proposed *WaveGraphNet* framework. The inverse edge set  $E_{\text{inv}}$  is induced by all measured paths in  $\mathcal{P}$ , whereas the forward edge set  $E_{\text{fwd}}$  is induced only by the selected paths in  $\mathcal{P}_f$ .

Graph component	Feature type	Definition
Node $v_i$	Node feature	Transducer coordinate $\mathbf{x}_i = \mathbf{r}_i$
Inverse edge $e_{ij}^{\text{inv}}, (i, j) \in E_{\text{inv}}$	Geometric features	Relative displacement $\mathbf{r}_j - \mathbf{r}_i$ , path length $\ \mathbf{r}_j - \mathbf{r}_i\ _2$
	Spectral features	Path-wise spectral descriptor $\mathbf{z}_{ij}$ containing normalized amplitudes and phase values over the selected frequency band
Forward edge $e_{ij}^{\text{fwd}}, (i, j) \in E_{\text{fwd}}$	Candidate Damage-geometric features	Relative displacement $\mathbf{r}_j - \mathbf{r}_i$ , path length $\ \mathbf{r}_j - \mathbf{r}_i\ _2$ , candidate-damage-to-source distance $\ \hat{\mathbf{p}} - \mathbf{r}_i\ _2$ , candidate-damage-to-target distance $\ \hat{\mathbf{p}} - \mathbf{r}_j\ _2$

For each inverse message-passing edge  $(i, j)$ , the edge features defined in Eq. (17) are composed of a geometric part and the spectral descriptor  $\mathbf{z}_{ij}$  from Eq. (8). We write the geometric part as

$$\mathbf{g}_{ij} = [\mathbf{r}_j - \mathbf{r}_i, \|\mathbf{r}_j - \mathbf{r}_i\|_2]. \quad (22)$$

Since not all spectral components are equally informative for localization, the edge encoder  $\phi_{\text{enc}}$  applies attention over  $\mathbf{z}_{ij}$  to compute a context vector for each edge,

$$\mathbf{c}_{ij} = \sum_{k=1}^K \alpha_{ij,k} \phi_{\text{feat}}(\mathbf{z}_{ij,k}), \quad (23)$$

where the attention weights are

$$\alpha_{ij,k} = \frac{\exp(\phi_{\text{attn}}(\mathbf{z}_{ij,k}))}{\sum_{m=1}^K \exp(\phi_{\text{attn}}(\mathbf{z}_{ij,m}))}. \quad (24)$$

The resulting spectral context is then combined with  $\mathbf{g}_{ij}$  to obtain the initial edge embedding,

$$\mathbf{h}_{ij}^{(0)} = \phi_{\text{enc}}(\mathbf{c}_{ij}, \mathbf{g}_{ij}). \quad (25)$$

Once the initial edge embeddings  $\mathbf{h}_{ij}^{(0)}$  have been obtained, node embeddings  $\mathbf{h}_i^{(0)}$  are computed from the corresponding transducer coordinates and combined with the aggregated embeddings of adjacent edges to form the input node representations:

$$\mathbf{x}_i^{(0)} = \phi_{\text{node}} \left( \mathbf{h}_i^{(0)}, \bigoplus_{j \in \mathcal{N}(i)} \mathbf{h}_{ji}^{(0)} \right), \quad (26)$$

where  $\bigoplus$  is a permutation-invariant aggregation operator, implemented here as the mean, and  $\phi_{\text{node}}$  combines the transducer embedding with the aggregated incoming edge information.

The model then applies a sequence of attention-based message-passing layers, updating the node representations at each layer  $\ell$ :

$$\mathbf{x}_i^{(\ell+1)} = \text{GAT}^{(\ell)} \left( \mathbf{x}_i^{(\ell)}, \{\mathbf{x}_j^{(\ell)}\}_{j \in \mathcal{N}(i)} \right) \quad (27)$$

The resulting node representations  $\{\mathbf{x}_i^{(L)}\}_{i=1}^N$  are pooled to obtain a graph-level embedding,

$$\mathbf{h}_{\mathcal{G}} = \text{Pool} \left( \{\mathbf{x}_i^{(L)}\}_{i=1}^N \right) \quad (28)$$

which is mapped to the predicted coordinate via the regression head  $\phi_{\text{reg}}$ :

$$\hat{\mathbf{p}} = \phi_{\text{reg}}(\mathbf{h}_{\mathcal{G}}) \quad (29)$$

While this inverse branch can learn meaningful localization patterns from data, it remains susceptible to ambiguous solutions, particularly in spatial regions not covered during training. The forward module is introduced to mitigate this limitation by encouraging consistency with the observed path-wise energy deviation response.

### 4.3. Forward consistency module

The forward module models the mapping from a candidate defect location to the path-wise energy-deviation pattern induced over the selected propagation paths. Specifically, it predicts the energy-deviation vector associated

with a given coordinate:

$$\widehat{\Delta \mathbf{E}} = g_\psi(\mathcal{G}_{\text{fwd}}(\hat{\mathbf{p}})), \quad (30)$$

where the forward graph shares the same node representation as the inverse graph but is induced only by the selected propagation-path subset  $\mathcal{P}_f$ . Its edge features are defined using geometric quantities relative to the hypothesized defect location. This module is intentionally lightweight: rather than reconstructing full guided-wave signals, it predicts only the path-wise energy-deviation quantities required for consistency evaluation. In doing so, it serves as a surrogate model of how a defect at a given location redistributes energy across the selected propagation paths.

Each forward message-passing edge feature  $\mathbf{e}_{ij}^{\text{fwd}}$ , with  $(i, j) \in E_{\text{fwd}}$ , is first embedded into a latent representation,

$$\mathbf{u}_{ij}^{(0)} = \phi_{\text{fwd,enc}}(\mathbf{e}_{ij}^{\text{fwd}}), \quad (31)$$

which is then processed by graph layers that propagate geometric context across the sensing network. Since the supervision target contains one scalar energy-deviation value per selected measured propagation path, the two message-passing directions associated with the same path are aggregated before decoding. For a selected path  $(i, j) \in \mathcal{P}_f$ , we write

$$\bar{\mathbf{u}}_{ij}^{(L)} = \bigoplus \left( \mathbf{u}_{ij}^{(L)}, \mathbf{u}_{ji}^{(L)} \right), \quad (32)$$

where  $\bigoplus$  denotes a permutation-invariant aggregation operator, implemented here as the mean. An edge-level decoder then predicts the energy deviation for the selected propagation path:

$$\widehat{\Delta E}_{ij} = \phi_{\text{fwd,dec}}(\bar{\mathbf{u}}_{ij}^{(L)}). \quad (33)$$

Collecting these predictions over all selected propagation paths yields

$$\widehat{\Delta \mathbf{E}} = \left[ \widehat{\Delta E}_{ij} \right]_{(i,j) \in \mathcal{P}_f}. \quad (34)$$

In this way, the forward module maps a candidate coordinate to the energy-deviation pattern it implies over the selected sensing paths. During training, discrepancies between this predicted pattern and the measured tar-

get  $\Delta\mathbf{E}$  are used to penalize inverse predictions that are inconsistent with the observed path-wise redistribution of guided-wave energy.

#### 4.4. Coupled training strategy

The model is trained in three sequential stages. In the first stage, the inverse branch learns an initial mapping from guided-wave measurements to defect coordinates. In the second stage, the forward branch is trained to predict the path-wise energy deviations associated with a given defect coordinate. In the final stage, both branches are coupled through a consistency objective, while only the inverse branch parameters are updated.

Throughout training, undamaged samples are assigned a fixed reference coordinate  $\mathbf{p}_{\text{ud}}$  located outside the admissible plate domain. This formulation enables damaged and undamaged samples to be handled within a unified coordinate-regression framework, eliminating the need for a separate damage-detection classifier.

*Stage I: inverse-branch pretraining.* In the first stage, only the inverse branch is trained. For damaged samples, the target corresponds to the true defect coordinate  $\mathbf{p}$ . For undamaged samples, the target is the out-of-domain reference coordinate  $\mathbf{p}_{\text{ud}}$ . The localization objective is defined as

$$\mathcal{L}_{\text{loc}} = \|\hat{\mathbf{p}} - \mathbf{p}\|_2^2, \quad (35)$$

where  $\mathbf{p}$  denotes the corresponding target coordinate for the sample, i.e., either the true defect location or the reference coordinate  $\mathbf{p}_{\text{ud}}$ . Both damaged and undamaged samples contribute to this objective. This stage establishes an initial coordinate predictor before introducing any forward-consistency constraint between the inverse and forward branches.

*Stage II: forward-branch pretraining.* In the second stage, the forward branch is trained on all training samples using the corresponding target coordinate to construct  $\mathcal{G}_{\text{fwd}}$ : the true defect coordinate for damaged samples and the out-of-domain reference coordinate  $\mathbf{p}_{\text{ud}}$  for undamaged samples. The optimization objective is formulated as a weighted mean squared error where each path-wise residual is scaled according to the observed energy deviation along the corresponding path. Specifically, the per-path weight is defined as

$$w_{ij}^{(n)} = \Delta E_{ij}^{(n)} + \epsilon, \quad (36)$$

where  $\epsilon = 0.01$  ensures strictly positive weights, including for paths where the observed deviation is zero. Consequently, paths exhibiting larger observed deviations contribute more strongly to the gradient signal during training, while unaffected paths receive proportionally smaller emphasis. The resulting training objective is defined as

$$\mathcal{L}_{\text{fwd}}^{\text{II}} = \frac{1}{N_{\text{tr}}|\mathcal{P}_{\text{f}}|} \sum_{n=1}^{N_{\text{tr}}} \sum_{(i,j) \in \mathcal{P}_{\text{f}}} \frac{w_{ij}^{(n)}}{w_{\text{min}}} \left( \widehat{\Delta E}_{ij}^{(n)} - \Delta E_{ij}^{(n)} \right)^2, \quad (37)$$

where  $w_{\text{min}} = \epsilon$  normalizes the weighting factors such that the minimum-weight contribution, corresponding to a completely unaffected path, contributes with unit weight. In contrast, a maximally affected path with  $\Delta E_{ij} = 1$  contributes with weight  $(1 + \epsilon)/\epsilon \approx 100$ . Consequently, the optimization process emphasizes paths exhibiting strong energy deviations, while still retaining a nonzero contribution from unaffected paths. For undamaged samples,  $\Delta E_{ij} \approx 0$  for all selected propagation paths in  $\mathcal{P}_{\text{f}}$ , implying that their contributions remain close to the minimum normalized weight of  $\epsilon/\epsilon = 1$ . As a result, their influence during optimization is comparatively small relative to damaged samples, whose affected paths may contribute weights up to approximately 100. At the end of this stage, the forward branch parameters are frozen and remain fixed throughout all subsequent training stages.

*Stage III: coupled optimization.* In the final stage, only the inverse branch is updated, while the pretrained forward branch is kept fixed and serves as a physics-guided consistency module. The overall training objective contains three components: a localization loss, a forward-consistency loss, and a physics-correction loss.

**Localization loss.** The localization loss is applied to both damaged and undamaged samples:

$$\mathcal{L}_{\text{loc}} = \|\hat{\mathbf{p}} - \mathbf{p}\|_2^2. \quad (38)$$

For damaged samples, this term supervises the predicted coordinate using the true defect location. For undamaged samples, the prediction is supervised against the out-of-domain reference coordinate  $\mathbf{p}_{\text{ud}}$ . This formulation preserves the ability of the inverse branch to consistently map undamaged

measurements to the designated reference coordinate outside the admissible spatial domain.

**Forward-consistency loss.** The forward-consistency loss is applied exclusively to damaged samples. In this stage, the forward graph  $\mathcal{G}_{\text{fwd}}$  is constructed using the predicted coordinate  $\hat{\mathbf{p}}$ , rather than the ground-truth coordinate. The frozen forward branch then predicts the energy-deviation pattern implied by this predicted location, which is subsequently compared with the observed energy-deviation pattern. Let  $\mathcal{D}$  denote the set of damaged training samples, the forward-consistency loss is then given by

$$\mathcal{L}_{\text{fwd}} = \frac{1}{|\mathcal{D}||\mathcal{P}_{\text{f}}|} \sum_{n \in \mathcal{D}} \sum_{(i,j) \in \mathcal{P}_{\text{f}}} \left( \widehat{\Delta E}_{ij}^{(n)} - \Delta E_{ij}^{(n)} \right)^2. \quad (39)$$

Since the forward branch remains frozen during this stage, gradients from  $\mathcal{L}_{\text{fwd}}$  propagate through the forward branch and update only the inverse branch. Consequently, the inverse branch is encouraged to predict coordinates whose implied energy-deviation patterns are compatible with the measured guided-wave response.

Undamaged samples are excluded from this objective because their energy deviations are approximately zero across the selected paths in  $\mathcal{P}_{\text{f}}$ , providing limited localization-specific consistency information.

**Physics-correction loss.** The physics-correction loss uses the frozen forward branch to estimate how the predicted coordinate should be adjusted in order to reduce the mismatch between predicted and observed energy deviations. For each damaged sample, we compute the gradient of the forward-consistency loss with respect to the predicted coordinate:

$$\hat{\mathbf{d}}^{(n)} = \frac{\nabla_{\hat{\mathbf{p}}^{(n)}} \mathcal{L}_{\text{fwd}}}{\|\nabla_{\hat{\mathbf{p}}^{(n)}} \mathcal{L}_{\text{fwd}}\|_2 + \varepsilon}. \quad (40)$$

where  $\hat{\mathbf{d}}^{(n)}$  defines a normalized direction in coordinate space along which the forward mismatch varies most strongly. In the implementation, this direction is computed using a detached coordinate-space probe, so that the correction direction is obtained from the frozen forward branch without introducing higher-order gradients through the inverse branch. A one-step physics-guided

correction is then applied to the predicted coordinate:

$$\hat{\mathbf{p}}_{\text{phys}}^{(n)} = \hat{\mathbf{p}}^{(n)} - \alpha \hat{\mathbf{d}}^{(n)}, \quad (41)$$

where  $\alpha$  controls the magnitude of the correction step. The corrected coordinate is subsequently supervised against the true defect location:

$$\mathcal{L}_{\text{corr}} = \frac{1}{|\mathcal{D}|} \sum_{n \in \mathcal{D}} \left\| \hat{\mathbf{p}}_{\text{phys}}^{(n)} - \mathbf{p}^{(n)} \right\|_2^2. \quad (42)$$

This objective encourages the inverse branch to generate predictions that are not only spatially close to the true defect location, but also geometrically consistent with the correction direction induced by the physics-correction branch. Intuitively, the predicted coordinate should lie in a region where a small physics-guided correction moves it toward the actual defect location.

As with the forward-consistency loss, undamaged samples are excluded from this term because their near-zero energy deviations do not provide informative localization gradients.

*Total objective.* The final optimization objective is defined as

$$\mathcal{L}_{\text{total}} = \mathcal{L}_{\text{loc}} + \lambda \mathcal{L}_{\text{fwd}} + \mu \mathcal{L}_{\text{corr}}. \quad (43)$$

where  $\mu$  is a fixed weighting coefficient for the physics-correction term. The forward-consistency weight  $\lambda$  is introduced progressively during training.  $\lambda$  is initialized to zero during a warmup phase of  $W$  epochs, during which optimization is driven solely by the localization objective. After the warmup period,  $\lambda$  is increased linearly until reaching a maximum value  $\lambda_{\text{max}}$ . This scheduling strategy prevents the frozen forward branch from dominating the optimization process during the early stages of training, when the inverse-branch predictions are still unstable.

*Model selection.* Model checkpoints are selected using a validation score computed on damaged validation samples:

$$s_{\text{val}} = \text{MSE}_{\text{loc}}^{\text{val}} + \text{MSE}_{\text{fwd}}^{\text{val}}. \quad (44)$$

The first term evaluates localization accuracy in coordinate space, while the second term assesses whether the predicted coordinates generate path-wise

energy-deviation patterns that remain consistent with the measured guided-wave response. Including the forward consistency term improves the robustness of checkpoint selection because it aggregates discrepancies across the selected  $|\mathcal{P}_f|$  propagation paths per sample, rather than relying exclusively on a single coordinate error. This additional structural information is particularly beneficial when the validation set contains only a limited number of distinct defect locations.

**Table 2:** Summary of the staged training strategy used in *WaveGraphNet*.  $\mathcal{D}$ : damaged training samples;  $\lambda$ : linearly scheduled weight (zero during warmup);  $\mu$ : fixed weight;  $\alpha$ : correction step size.

Stage	Updated module	Samples used	Objective
I	Inverse branch	All (damaged + undamaged)	$\mathcal{L}_{\text{loc}} = \ \hat{\mathbf{p}} - \mathbf{p}\ _2^2$
II	Forward branch	All (damaged + undamaged; damaged paths dominate via focus weight)	$\mathcal{L}_{\text{fwd}}^{\text{II}}$ : focus-weighted MSE on path-wise energy deviation using ground-truth coordinate
III	Inverse branch only (forward branch fixed)	$\mathcal{L}_{\text{loc}}$ : all samples $\mathcal{L}_{\text{fwd}}, \mathcal{L}_{\text{corr}}$ : damaged only ( $\mathcal{D}$ )	$\mathcal{L}_{\text{total}} = \mathcal{L}_{\text{loc}} + \lambda \mathcal{L}_{\text{fwd}} + \mu \mathcal{L}_{\text{corr}}$ where $\mathcal{L}_{\text{corr}}$ supervises $\hat{\mathbf{p}} - \alpha \hat{\mathbf{d}}$ against the true coordinate

#### 4.5. Inference pipeline

During inference, defect localization is performed solely using the inverse branch:

$$\hat{\mathbf{p}} = f_{\theta}(\mathcal{G}_{\text{inv}}). \quad (45)$$

The forward branch is not required during deployment and primarily serves as a physics-guided regularizer during training. Optionally, it may be evaluated post hoc to verify whether the predicted coordinate yields an energy-deviation pattern that is consistent with the measured guided-wave response. As a result, *WaveGraphNet* maintains a simple and computationally efficient

inference pipeline. Once the graph representation has been constructed from the measured guided-wave data, localization requires only a single forward pass through the inverse branch.

## 5. Case study: Guided-wave localization in CFRP plates

The proposed framework is evaluated on the openly available Open Guided Waves benchmark dataset, referred to here as OGW-1, for guided-wave structural health monitoring on a composite plate [32]. This dataset was collected and published independently of the present study, and full experimental details are provided in the original benchmark paper [32]. OGW-1 is an openly available guided-wave benchmark platform and was not specifically designed for the present study. For the present evaluation, we define two spatial hold-out splits on this dataset with increasing extrapolation difficulty. Both splits serve as controlled experimental testbeds for assessing whether the proposed inductive bias improves localization performance in unseen damage regions under limited spatial training coverage, rather than for demonstrating broad statistical coverage of operating conditions.

### 5.1. Problem setup

The specimen is a quasi-isotropic CFRP plate representative of lightweight aerospace structures. It is manufactured from *Hexply*<sup>®</sup> *M21/34%/UD134/T700/300* prepreg material, has nominal dimensions of  $500 \times 500$  mm<sup>2</sup> and a thickness of 2 mm. The laminate consists of 16 plies arranged in a symmetric and balanced stacking sequence  $[45^\circ/0 - 45^\circ/90]_s$ , providing quasi-isotropic in-plane stiffness through equal representation of 0,  $\pm 45$ , and 90 fiber orientations. The plate is instrumented with 12 co-bonded DuraAct piezoelectric transducers arranged in two rows along the plate boundaries, yielding a sparse edge-mounted sensing layout typical of large-area monitoring applications [4]. Each transducer has a diameter of 5 mm and a thickness of 0.2 mm.

Measurements are acquired in pitch-catch mode, in which one transducer excites the plate and another records the received response. As a result, localization must be inferred from path-wise perturbations across the sensor network rather than from full-field wavefield measurements. To enable repeatable damage scenarios without permanently modifying the specimen, the benchmark uses a reversible pseudo-defect consisting of an aluminum disk attached with tacky tape. This surrogate does not reproduce every aspect of

real in-service damage, but it does create repeatable local scattering, attenuation, and travel-time perturbations suitable for benchmarking localization algorithms under controlled conditions.

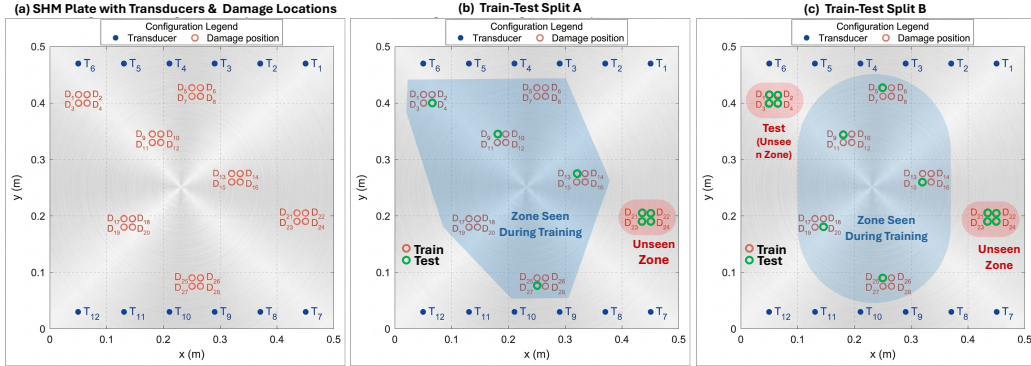


**Figure 2: OGW-1 SHM Plate and spatial train–test splits.** (a) CFRP plate with 12 boundary-mounted transducers and 28 defect locations. (b) Split A: held-out test zone ( $D_{21}$ – $D_{24}$ , red) lies at the boundary of the training region. (c) Split B: held-out test zone comprises two corner clusters ( $D_1$ – $D_4$  and  $D_{21}$ – $D_{24}$ , red), both lying outside the training coverage, making it the more challenging extrapolation setting.

## 5.2. Dataset construction and preprocessing

For each experiment, one transducer acts as an actuator, and responses are recorded for the remaining channels, producing the path-wise signals  $s_{ij}(t)$  introduced in Section 3. As described in the OGW-1 acquisition protocol [32], each unordered transducer pair is measured only once; consequently,  $(i, j)$  and  $(j, i)$  are not considered distinct observations. For a system with 12 transducers, this results in 66 unique propagation paths per sample. Accordingly, each sample is represented on a fixed graph topology, with fixed node coordinates and a consistent set of path-wise measurements throughout the study.

The campaign comprises repeated pristine acquisitions as well as measurements obtained by placing a pseudo-defect at multiple spatial locations. In line with the scope of this study, only single-defect cases are considered. Multi-defect examples available in the repository are excluded, as the learning target is a single coordinate  $\mathbf{p} \in \Omega$  per sample. After this filtering,

the resulting dataset consists of 28 damaged samples and 60 pristine samples. While these sample sizes are small by conventional machine-learning standards, they are appropriate for the present study, which is to compare modeling choices under controlled data-scarcity conditions rather than to demonstrate saturated benchmark performance.

Prior to feature extraction, the raw voltage traces are high-pass filtered using a third-order Butterworth filter with a cutoff frequency of 20 kHz in order to suppress low-frequency drift and background components while preserving the guided-wave content around the selected 100 kHz excitation band. The analysis is restricted to measurements acquired at excitation frequency 100 kHz. Each retained sample is initially represented as a  $13,108 \times 66$  matrix of time-domain guided-wave measurements, where 13,108 denotes the number of temporal samples per propagation path and 66 corresponds to the number of unique paths induced by the 12-transducer configuration. A path-wise pristine reference signal,  $\bar{s}_{ij}(t)$ , is estimated from the healthy measurements and subtracted from each sample to obtain the differential response defined in Eq. (6). The same reference construction procedure is applied consistently across all samples, ensuring that damaged measurements are compared against a common healthy baseline. The resulting differential signals are subsequently transformed into the frequency domain to construct the descriptors  $\mathbf{z}_{ij}$  in Eq. (8). Amplitude normalization is performed using statistics computed exclusively from the training data without incorporating information from the held-out defect regions during the normalization process.

For the forward branch, the observed consistency target  $\Delta\mathbf{E}$  is computed from the damaged and pristine spectral amplitudes using Eq. (12) over the same frequency band. This results in a scalar energy-deviation value for each selected propagation path and defines the path-wise supervision target used in the coupled training objective. The forward consistency target is computed only over the selected propagation-path subset  $\mathcal{P}_f$ , whereas the inverse branch uses all measured propagation paths in  $\mathcal{P}$ . Thus, the two branches share the same transducer layout but differ in their edge sets, supervision targets, and edge feature definitions.

### 5.3. Train–test protocol and evaluation setting

We evaluate the proposed method using two spatial hold-out splits with increasing extrapolation difficulty, both illustrated in Fig. 2. In Split A, the held-out test region consists of four damage locations,  $D_{21}$ – $D_{24}$ , located near

the boundary of the spatial region covered by the training samples. In Split B, the held-out test regions comprise two corner clusters,  $D_1$ – $D_4$  and  $D_{21}$ – $D_{24}$ , both of which lie outside the spatial extent spanned by the training damage locations. Consequently, Split B represents a substantially more challenging spatial extrapolation scenario.

For both splits, all repeated measurements associated with the held-out damage locations are assigned exclusively to the test set and are never mixed with the training data. This protocol is intentionally more stringent than random partitioning, as it evaluates extrapolation to unseen spatial regions rather than interpolation between nearby observed locations. It therefore more closely reflects the deployment gap emphasized in SHM, where laboratory evaluations often overestimate performance in configurations not encountered during development [2].

Training is performed using damaged samples from the observed spatial regions together with the undamaged samples assigned to the training split. During training, undamaged samples are incorporated into the same regression framework by assigning them a virtual target coordinate  $\mathbf{p}_{\text{ud}}$  located outside the admissible plate domain. This design eliminates the need for a separate damage-detection classifier and ensures that all models solve a unified coordinate-regression problem. Normalization statistics are computed using training data only, and all baseline models use the same data split and preprocessing pipeline.

During testing, damaged samples from the held-out spatial regions are used to evaluate localization accuracy, while undamaged samples are included to assess false-positive behavior. For undamaged test samples, we report the false positive rate (FPR), defined as the fraction of undamaged samples that are incorrectly mapped to an admissible damage location.

Localization performance is evaluated by comparing the predicted coordinate  $\hat{\mathbf{p}}$  with the ground-truth defect coordinate  $\mathbf{p}$  for held-out damaged samples. Localization errors are reported both in normalized coordinate space and as mean absolute error (MAE) in millimeters. In addition, undamaged test samples are used to evaluate the false positive rate (FPR), defined as the fraction of undamaged measurements that are incorrectly mapped to an admissible damage location. Results are reported separately for the seen region, whose damage locations lie within the spatial coverage of the training data, and for the unseen held-out test regions defined in Split A and Split B.

Given the limited number of distinct test locations, the reported quantitative results should be interpreted primarily as indicators of relative model

behavior under a common evaluation protocol, rather than as comprehensive estimates of real-world performance. Moreover, the spatially held-out evaluation setting is also distinct from many previous studies on this benchmark, which do not explicitly assess localization in extrapolation regions outside the spatial coverage of the training data. Accordingly, the discussion focuses on relative model ranking, characteristic error patterns, and train–test generalization gaps rather than nominal percentage improvements.

**Table 3:** Architecture summary for all compared models.  $d$ : hidden dimension; *Pool*: graph-level aggregation operator; BiLSTM: bidirectional long short-term memory; MP: message-passing layer; GAT: graph attention network layer; Layer-Norm: layer normalization; ELU: exponential linear unit.

Model	Encoder	Processor	$d$	Layers $\times$ Heads	Pool
1D-CNN	5-block Conv1d (16 $\rightarrow$ 256, kernel 3, ReLU, MaxPool)	—	256	5 conv	AvgPool
LSTM	—	3-layer BiLSTM + self-attention	256	3 BiLSTM	Self- attn
GNN-MLP	4-layer MLP (static edge)	MP, mean aggregation	256	4 MP	Mean
GAT	4-layer MLP (static edge)	GAT	256	4 GAT $\times$ 16	Attn.
<i>WGN</i> (inv.)	Freq.-bin attention, $K=256$ bins per edge	GAT + LayerNorm + ELU	256	4 GAT $\times$ 16	Max
<i>WGN</i> (fwd.)	MLP on geometric edge features	MP with residual connections	128	3 MP	Edge

All models use a 3-layer MLP regression head predicting the 2D defect coordinate, except *WGN* (fwd.) whose decoder outputs  $\widehat{\Delta\mathbf{E}} \in \mathbb{R}^{36}$  via a 2-layer MLP with Softplus activation. Dropout: LSTM 0.3, *WGN* (inv.) 0.2, all others 0.

## 6. Implementation details and model configurations

This section describes the experimental implementation and comparative evaluation setup used to assess the proposed framework. The localization problem formulation, graph construction procedure, coupled inverse–forward

architecture, and training objectives were introduced in Sections 3 and 4, while Sections 5–5.3 detailed the dataset, preprocessing pipeline, spatial hold-out protocol, and evaluation metrics. Here, we focus specifically on the implementation choices required to reproduce the experiments and on the configurations of the compared models.

All models are trained and evaluated using the same preprocessing pipeline, frequency-band selection, normalization procedure, spatial split definitions, and random seeds. This ensures that observed performance differences arise from the model architecture and training objectives rather than from variations in data preparation. The comparison includes two non-graph baselines, two graph-based baselines, the inverse-only version of *WaveGraphNet*, and the full coupled *WaveGraphNet* model.

The non-graph baselines, namely the one-dimensional convolutional neural network (1D-CNN) [33] and long short-term memory network (LSTM) [34], operate on ordered path-wise inputs without explicitly encoding the transducer-network geometry. In contrast, the graph-based baselines, namely the graph neural network with multilayer-perceptron edge encoder (GNN-MLP) [35] and the graph attention network (GAT) [16], use the same inverse graph representation as *WaveGraphNet* but are trained solely with the coordinate localization objective.

To isolate the effect of the proposed physics-guided coupling, we additionally evaluate inverse-only *WaveGraphNet*, which uses the proposed inverse architecture without the forward-consistency branch. The full coupled model extends this formulation by incorporating the frozen forward branch during the final training stage to impose the forward-consistency and physics-correction objectives.

Hyperparameters were selected by random search on the validation set, without using the spatially held-out test regions. The same validation-based selection procedure and comparable search budget were used for all baseline models and for *WaveGraphNet*. The final selected architectural configurations for all compared models are summarized in Table 3, while the shared optimization settings, spatial split definitions, and stage-wise training schedule for *WaveGraphNet* are provided in Table 4.

**Table 4:** Training protocol shared across all models and stage-specific settings for *WaveGraphNet*. *Seen zone*: damage locations within the spatial extent of the training data, used for validation and seen-zone evaluation. *Unseen zone*: held-out damage locations outside the training coverage, used for test evaluation only.

Setting	Value
<i>Shared across all models</i>	
Optimizer	Adam, $\eta = 10^{-4}$
LR schedule	ReduceLROnPlateau (factor 0.8, patience 20)
Batch size	8
Total epochs	900
Seeds	{0, 1, 42}
Frequency band	256 bins, 69.4–128 kHz (FFT)
<i>WaveGraphNet stage schedule (900 ep total)</i>	
Stage I (inv. pretrain)	150 ep, $\eta=10^{-4}$ , loss: $\mathcal{L}_{\text{loc}}$
Stage II (fwd. pretrain)	150 ep, $\eta=10^{-4}$ , loss: $\mathcal{L}_{\text{fwd}}^{\text{II}}$ (focus-weighted)
Stage III (coupled)	600 ep, $\eta=10^{-5}$ , loss: $\mathcal{L}_{\text{loc}} + \lambda\mathcal{L}_{\text{fwd}} + \mu\mathcal{L}_{\text{corr}}$
$\lambda$ schedule	0 for first 40 warmup ep, then linear ramp to $\lambda_{\text{max}}=3$
$\mu, \alpha$	$\mu=1.0, \alpha=0.1$
Checkpoint score	$s_{\text{val}} = \text{MSE}_{\text{loc}}^{\text{val}} + \text{MSE}_{\text{fwd}}^{\text{val}}$ (damaged val samples only)

## 7. Results

This section evaluates *WaveGraphNet* on the OGW-1 SHM Plate benchmark under the spatially held-out protocol defined in Section 5.3. Results are reported for two extrapolation scenarios of increasing difficulty. In Split A, the held-out damage region is located near the boundary of the spatial domain covered during training. In Split B, two corner regions are excluded from training while the observed damage locations remain concentrated in the central region of the plate, resulting in a substantially more challenging extrapolation setting. Quantitative results are averaged over three random seeds to reduce sensitivity to initialization effects. In addition, representative localization maps are provided to visualize the spatial structure of the prediction errors and the generalization behavior of the compared models in unseen regions.

### 7.1. Aggregate performance across spatial splits

The aggregate results evaluate how well the compared models generalize from observed damage regions to spatially unseen defect locations under the two extrapolation settings, Split A and Split B. In particular, the comparison distinguishes between localization performance within the spatial coverage of the training data and performance in held-out regions outside that coverage, thereby directly assessing spatial extrapolation capability.

Table 5 summarizes the corresponding localization errors for all compared models. The seen-zone MAE is computed on damage locations lying within the spatial region covered during training, whereas the unseen-zone MAE is evaluated on held-out damage locations outside the training coverage. All MAE values are normalized by the plate dimension of 500 mm. Consequently, a normalized MAE of 0.220 corresponds to an average localization error of approximately 110 mm. The false positive rate (FPR) is computed using six held-out undamaged test samples evaluated across three random seeds, resulting in a total of 18 undamaged evaluation cases.

The aggregate results reveal two consistent trends across both spatial extrapolation settings. First, all models exhibit a clear degradation in performance when moving from the within-coverage regions to the spatially unseen test regions. As shown in Fig. 3, unseen-zone errors are consistently higher than seen-zone errors, confirming that the proposed evaluation protocol measures extrapolation beyond the observed damage grid rather than interpolation within previously observed regions. This train-test gap becomes substantially larger in Split B, where the held-out regions lie outside a more spatially restricted central training coverage, making the extrapolation problem considerably more challenging.

Second, the comparison shows that architectural inductive bias has a strong influence on extrapolation behavior. Among the non-graph baselines, the 1D-CNN consistently outperforms the LSTM, achieving lower unseen-zone MAE in both Split A and Split B. The GNN-MLP baseline does not consistently improve over the 1D-CNN, indicating that incorporating graph structure alone is insufficient to guarantee better spatial generalization. In contrast, the attention-based GAT baseline achieves a lower unseen-zone error than both GNN-MLP and 1D-CNN across both splits. This suggests that explicitly encoding the sensing graph becomes more effective when the model can adaptively weight propagation paths according to their relevance. The proposed *WaveGraphNet* variants further improve upon these baselines; the full coupled model achieves the lowest errors in both extrapolation settings,

**Table 5:** Localization performance on the OGW-1 benchmark under two spatial hold-out splits, reported as mean  $\pm$  std across three seeds  $\{0, 1, 42\}$ . *Seen MAE*: error on the in-coverage test set (damage zones within training spatial coverage). *Unseen MAE*: error on the held-out test set (damage zones outside training coverage). MAE values are normalized by the plate dimension (500 mm). *FPR*: false positive rate on 6 held-out undamaged test samples across 3 seeds, giving 18 evaluations in total. The best-performing model for each metric is shown in bold, and the second-best is underlined.

Model	Seen MAE	Unseen MAE	FPR
<i>Split A — one unseen zone outside the training spatial coverage</i>			
1D CNN	0.107 $\pm$ 0.009	0.326 $\pm$ 0.021	38.9% <sub>(7/18)</sub>
LSTM	0.432 $\pm$ 0.008	0.489 $\pm$ 0.020	77.8% <sub>(14/18)</sub>
GNN-MLP	0.260 $\pm$ 0.012	0.355 $\pm$ 0.015	66.7% <sub>(12/18)</sub>
GAT	0.075 $\pm$ 0.011	0.305 $\pm$ 0.005	55.6% <sub>(10/18)</sub>
WGN (Inverse Only)	<b>0.046 <math>\pm</math> 0.005</b>	<u>0.255 <math>\pm</math> 0.033</u>	33.3% <sub>(6/18)</sub>
WGN (Coupled)	0.079 $\pm$ 0.015	<b>0.220 <math>\pm</math> 0.027</b>	<b>0.0%</b> <sub>(0/18)</sub>
<i>Split B — two unseen zones outside smaller training coverage (harder)</i>			
1D CNN	0.098 $\pm$ 0.002	0.397 $\pm$ 0.020	16.7% <sub>(3/18)</sub>
LSTM	0.288 $\pm$ 0.018	0.516 $\pm$ 0.042	94.4% <sub>(17/18)</sub>
GNN-MLP	0.244 $\pm$ 0.010	0.438 $\pm$ 0.007	66.7% <sub>(12/18)</sub>
GAT	0.102 $\pm$ 0.019	0.383 $\pm$ 0.010	33.3% <sub>(6/18)</sub>
WGN (Inverse Only)	<b>0.072 <math>\pm</math> 0.009</b>	<u>0.328 <math>\pm</math> 0.015</u>	<b>0.0%</b> <sub>(0/18)</sub>
WGN (Coupled)	0.097 $\pm$ 0.019	<b>0.262 <math>\pm</math> 0.016</b>	<b>0.0%</b> <sub>(0/18)</sub>

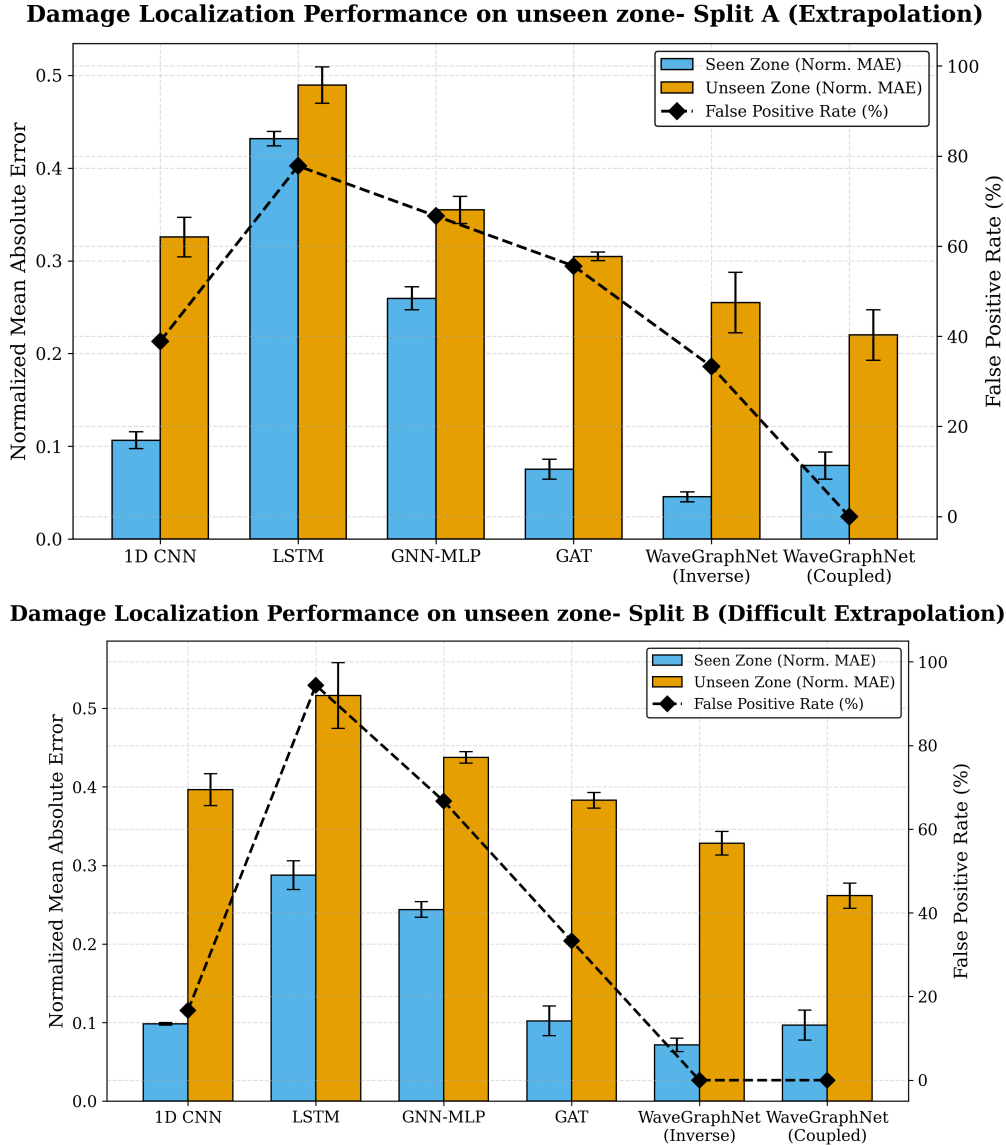


**Figure 3: Comparison of localization errors across baseline models.** Estimated localization errors for the non-graph baselines, the generic graph baselines, *WaveGraphNet (Inverse-only)*, and the full *WaveGraphNet* framework.

reducing the unseen-zone MAE from  $0.305 \pm 0.005$  to  $0.220 \pm 0.027$  relative to GAT in Split A, and from  $0.383 \pm 0.010$  to  $0.262 \pm 0.016$  in Split B.

These improvements indicate that coupling inverse localization with forward-consistency constraints provides additional regularization that improves spatial generalization in previously unseen damage regions.

Within the proposed framework, the inverse-only *WaveGraphNet* achieves the lowest seen-zone MAE in both splits, with normalized errors of  $0.046 \pm 0.005$  in Split A and  $0.072 \pm 0.009$  in Split B. This indicates that the inverse architecture alone is highly effective at fitting damage locations within the spatial support of the training data. However, the full coupled model achieves the best performance in the held-out spatial regions, reducing the unseen-zone MAE from  $0.255 \pm 0.033$  to  $0.220 \pm 0.027$  in Split A and from  $0.328 \pm 0.015$  to  $0.262 \pm 0.016$  in Split B. These results indicate that the primary contribution of the forward-consistency coupling is not improved interpolation within observed regions, but improved extrapolation to spatially unseen damage locations.

Finally, the dashed FPR curve in Fig. 3 shows that several models incorrectly map some undamaged measurements into the admissible damage region. The LSTM has the highest FPR in both splits, while the 1D-CNN, GNN-MLP, and GAT show split-dependent false-positive behavior. In contrast, the coupled *WaveGraphNet* achieves an FPR of 0.0% in both extrapolation settings while simultaneously obtaining the lowest unseen-zone MAE. This suggests that the coupled formulation improves localization performance in held-out damage regions without compromising the model’s ability to map undamaged measurements to the out-of-domain no-damage reference coordinate.

### 7.2. Representative localization behavior

To complement the aggregate results, we next examine representative localization maps from Split A for the proposed framework and the baseline models. These visualizations correspond to a single random seed and are intended to illustrate the qualitative spatial structure of the prediction errors rather than provide additional quantitative evaluation.

Figure 4 illustrates the representative behavior of *WaveGraphNet (Inverse-only)*. The model accurately localizes damage locations within the seen region and maps the undamaged sample close to the designated no-damage reference coordinate. In the unseen region, however, the predicted locations remain partially biased toward the spatial support of the training data, illustrating the limitations of coordinate-only supervision for extrapolation beyond observed damage regions.

Performance of WaveGraphNet Framework-  
*Inverse Only Model*  
**Split-A Representative Test Set**

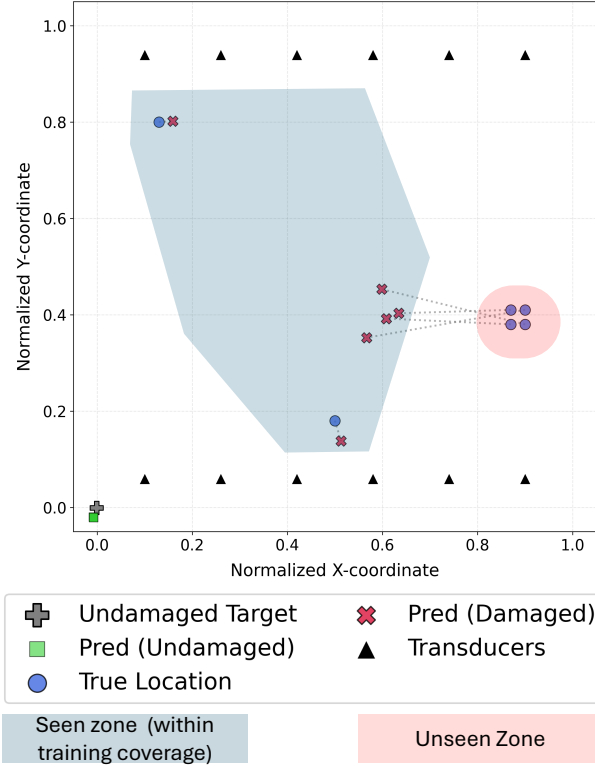


**Figure 4: Representative predictions of *WaveGraphNet (Inverse-only)*.** Damage localization results for the test set consisting of seen and unseen damage zones (from the spatially held-out region). Blue circles denote true damage locations, red crosses denote predicted damaged locations, green squares denote predicted undamaged locations, the gray marker denotes the no-damage target  $\mathbf{p}_{ud} = [-0.001, -0.001]$ , and black triangles denote transducer locations.

Figure 5 shows the corresponding localization result for the full coupled *WaveGraphNet* model. Compared with the inverse-only variant, the predictions in the unseen region are more concentrated around the true held-out damage locations, with substantially reduced spatial bias toward the training region. This qualitative behavior is consistent with the improved extrapolation performance reported in Section 7.1 and suggests that the forward-consistency coupling improves spatial extrapolation beyond the observed

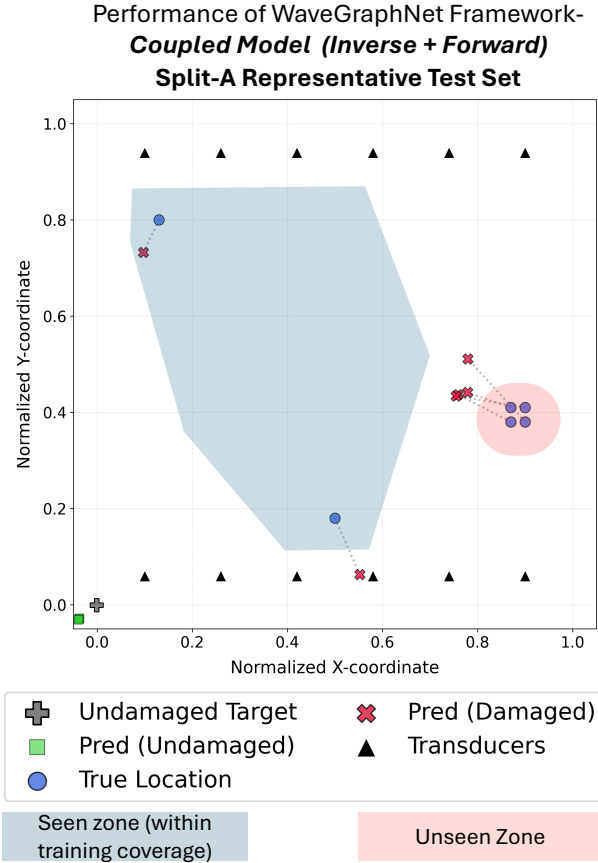


**Figure 5: Representative predictions of the coupled *WaveGraphNet* model.** Damage localization results for the test set consisting of seen and unseen damage zones (from the spatially held-out region). Blue circles denote true damage locations, red crosses denote predicted damaged locations, green squares denote predicted undamaged locations, the gray marker denotes the no-damage target  $\mathbf{p}_{ud} = [-0.001, -0.001]$ , and black triangles denote transducer locations.

damage domain.

Figure 6 presents the corresponding baseline predictions for the same representative setting. Among the non-graph baselines, the 1D-CNN produces more spatially concentrated predictions than the LSTM, whereas the LSTM exhibits visibly dispersed localization patterns and frequently maps undamaged samples into the admissible damage region. The GNN-MLP baseline also shows substantial prediction spread in the unseen region. The attention-

## Performance of Baselines on **Split-A** Representative Test Set

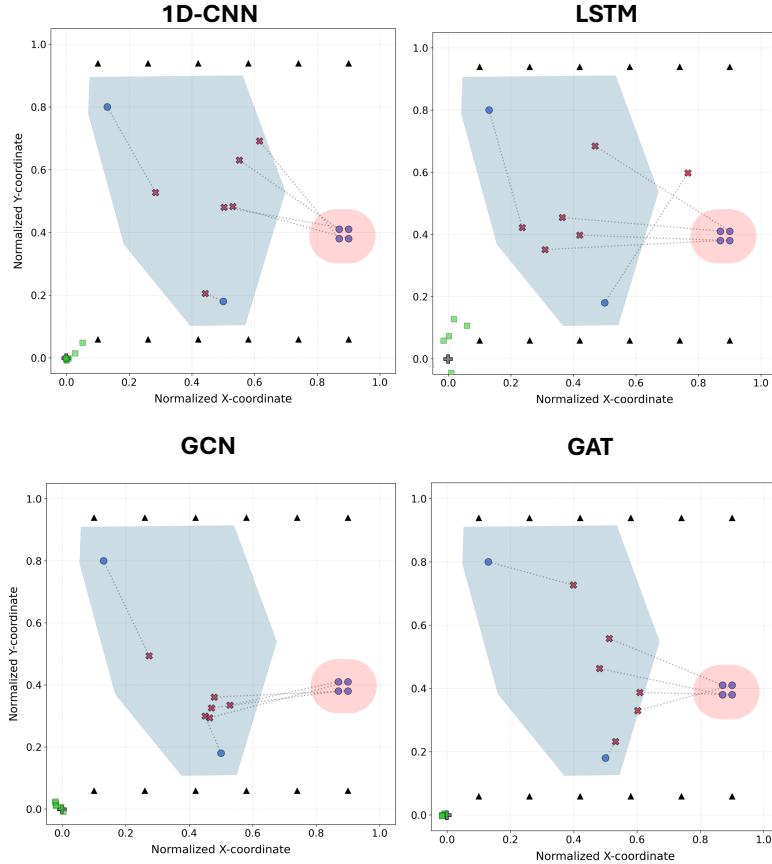


**Figure 6: Localization behavior of the baseline models.** Blue circles denote true damage locations, red crosses denote predicted damaged locations, green squares denote predicted undamaged locations, the gray marker denotes the no-damage target  $\mathbf{p}_{\text{ud}} = [-0.001, -0.001]$ , and black triangles denote transducer locations.

based GAT baseline gives a more structured and spatially coherent prediction pattern, indicating that adaptive weighting of propagation paths improves generalization relative to the simpler graph formulation. Nevertheless, the coupled *WaveGraphNet* remains the most spatially concentrated and geometrically consistent model in the held-out region.

Overall, the quantitative and qualitative results indicate that the cou-

pled *WaveGraphNet* provides the most reliable performance under the spatial hold-out protocol considered in this study. The model achieves the lowest unseen-zone localization error in both extrapolation settings while maintaining a zero false-positive rate on held-out undamaged samples. These findings suggest that coupling inverse localization with forward energy-deviation consistency improves extrapolation to spatially unseen damage regions, particularly under limited spatial training coverage of the monitored structure.

## 8. Conclusion

This paper proposed *WaveGraphNet*, a coupled inverse–forward graph learning framework for guided-wave damage localization in CFRP plates that integrates relational graph modeling with physics-guided forward consistency constraints. *WaveGraphNet* models the sparse transducer network as a graph and predicts defect coordinates directly from graph-structured guided-wave measurements. In contrast to purely inverse localization approaches, the framework introduces a learned forward-consistency mechanism that regularizes the predicted coordinates by encouraging consistency between the inferred defect location and the corresponding path-wise energy-deviation pattern.

The framework was evaluated on the OGW-1 SHM Plate benchmark using the spatial hold-out protocol introduced in this work, which explicitly tests extrapolation to unseen damage regions outside the spatial coverage of the training data. Across both evaluated extrapolation settings, the coupled *WaveGraphNet* achieved the lowest unseen-zone localization error among all compared baselines. The improvement became more pronounced in the more challenging Split B setting, where two corner regions were excluded from training and the observed damage locations were concentrated centrally. In addition, the coupled model achieved a zero false-positive rate on held-out undamaged samples in both splits, demonstrating that improved extrapolation performance did not come at the expense of degraded no-damage behavior.

These results provide evidence that sparse guided-wave localization benefits from combining relational graph representations with physics-guided forward-consistency constraints. The graph formulation captures the distributed structure of the sensing network, while the forward branch constrains the inverse solution space by penalizing coordinate predictions whose implied path-wise energy redistribution is inconsistent with the measured guided-wave response. This coupled formulation reduces ambiguity in the

inverse localization problem and improves spatial generalization under limited spatial training coverage.

More broadly, the proposed framework highlights the potential of combining learned inverse mappings with differentiable forward consistency mechanisms for SHM localization tasks where direct supervision is spatially sparse and extrapolation is required. The results further demonstrate that evaluation protocols based solely on random train–test splits may substantially overestimate localization performance relative to more realistic spatially held-out scenarios.

The present study should nevertheless be interpreted as a controlled experimental case study on the OGW-1 SHM Plate dataset rather than as a comprehensive deployment validation. Future work will extend the framework to additional specimens, damage types, environmental and operational variability, and repeated spatial partitioning protocols. An important next step is to evaluate the robustness of the proposed coupling mechanism under environmental variability, sensor drift, and changing boundary conditions, which remain major challenges for guided-wave SHM in practice. Future research will also investigate uncertainty-aware localization, multi-defect scenarios, and more general physics-guided graph learning formulations for guided-wave structural health monitoring.

**Code and Data Availability:** The *WaveGraphNet* implementation will be made publicly available in an open-source repository, including preprocessing scripts, graph-construction code, training configurations, and the spatial hold-out split definitions used in this study. The released splits include both Split A and Split B for the OGW-1 SHM Plate benchmark. The raw OGW-1 dataset is publicly available from the original benchmark source [32].

**Acknowledgment:** This research was funded by the Swiss National Science Foundation (SNSF) Grant Number 200021\_200461.

**Declaration of Generative AI and AI-assisted technologies in the writing process:** During the preparation of this work, the authors used ChatGPT to assist with refining and correcting the text. After using this tool, the authors carefully reviewed and edited the content as needed and take full responsibility for the content of this publication.

## References

- [1] A. Güemes, A. Fernandez-Lopez, A. R. Pozo, J. Sierra-Perez, Structural health monitoring for advanced composite structures: A review, *Journal of Composites Science* 4 (1) (2020) 13. doi:10.3390/jcs4010013.
- [2] P. Cawley, Structural health monitoring: Closing the gap between research and industrial deployment, *Structural Health Monitoring* 17 (5) (2018) 1225–1244. doi:10.1177/1475921717750047.
- [3] F. Ricci, E. Monaco, N. D. Boffa, L. Maio, V. Memmolo, Guided waves for structural health monitoring in composites: A review and implementation strategies, *Progress in Aerospace Sciences* 129 (2022) 100790. doi:10.1016/j.paerosci.2021.100790.
- [4] L. Capineri, A. Bulletti, Ultrasonic guided-waves sensors and integrated structural health monitoring systems for impact detection and localization: A review, *Sensors* 21 (9) (2021) 2929. doi:10.3390/s21092929.
- [5] M. Philibert, K. Yao, M. Gresil, C. Soutis, Lamb waves-based technologies for structural health monitoring of composite structures for aircraft applications, *European Journal of Materials* 2 (1) (2022) 436–474. doi:10.1080/26889277.2022.2094839.
- [6] P. Cawley, Guided waves in long range nondestructive testing and structural health monitoring: Principles, history of applications and prospects, *NDT & E International* 142 (2024) 103026. doi:10.1016/j.ndteint.2023.103026.
- [7] M. Tanveer, M. U. Elahi, J. Jung, M. M. Azad, S. Khalid, H. S. Kim, Recent advancements in guided ultrasonic waves for structural health monitoring of composite structures, *Applied Sciences* 14 (23) (2024) 11091. doi:10.3390/app142311091.
- [8] A. Sattarifar, T. Nestorović, Emergence of machine learning techniques in ultrasonic guided wave-based structural health monitoring, *International Journal of Prognostics and Health Management* 13 (1) (2022). doi:10.36001/ijphm.2022.v13i1.3107.
- [9] Y. Liao, X. Qing, Y. Wang, F. Zhang, Damage localization for composite structure using guided wave signals with gramian angular field image

- coding and convolutional neural networks, *Composite Structures* 312 (2023) 116871. doi:10.1016/j.compstruct.2023.116871.
- [10] Y. Gao, L. Sun, R. Song, C. Peng, X. Wu, J. Wei, M. Jiang, Q. Sui, L. Zhang, Damage localization in composite structures based on lamb wave and modular artificial neural network, *Sensors and Actuators A: Physical* 370 (2024) 115644. doi:10.1016/j.sna.2024.115644.
- [11] M. M. Azad, O. Munyaneza, J. Jung, J. W. Sohn, J.-W. Han, H. S. Kim, Damage localization and severity assessment in composite structures using deep learning based on lamb waves, *Sensors* 24 (24) (2024) 8057. doi:10.3390/s24248057.
- [12] L. Lomazzi, M. Giglio, F. Cadini, Towards a deep learning-based unified approach for structural damage detection, localisation and quantification, *Engineering Applications of Artificial Intelligence* 121 (2023) 106003. doi:10.1016/j.engappai.2023.106003.
- [13] F. Scarselli, M. Gori, A. C. Tsoi, M. Hagenbuchner, G. Monfardini, The graph neural network model, *IEEE Transactions on Neural Networks* 20 (1) (2009) 61–80. doi:10.1109/TNN.2008.2005605.
- [14] J. Gilmer, S. S. Schoenholz, P. F. Riley, O. Vinyals, G. E. Dahl, Neural message passing for quantum chemistry, *Proceedings of the 34th International Conference on Machine Learning* 70 (2017) 1263–1272.
- [15] T. N. Kipf, M. Welling, Semi-supervised classification with graph convolutional networks, in: *International Conference on Learning Representations*, 2017.  
URL <https://openreview.net/forum?id=SJU4ayYgl>
- [16] P. Veličković, G. Cucurull, A. Casanova, A. Romero, P. Liò, Y. Bengio, Graph attention networks, in: *International Conference on Learning Representations*, 2018.  
URL <https://openreview.net/forum?id=rJXMpikCZ>
- [17] V. Sharma, O. Fink, A physics-informed graph neural network conserving linear and angular momentum for dynamical systems, *Nature Communications* (2026).

- [18] S. Bloemheuvel, J. van den Hoogen, M. Atzmueller, A computational framework for modeling complex sensor network data using graph signal processing and graph neural networks in structural health monitoring, *Applied Network Science* 6 (1) (2021). doi:10.1007/s41109-021-00438-8.
- [19] M. A. Cheema, M. Z. Sarwar, V. C. Gogineni, D. Cantero, P. S. Rossi, Computationally efficient structural health monitoring using graph signal processing, *IEEE Sensors Journal* 24 (7) (2024) 11895–11905. doi:10.1109/JSEN.2024.3366346.
- [20] S. Wang, Z. Luo, P. Shen, H. Zhang, Z. Ni, Graph-in-graph convolutional network for ultrasonic guided wave-based damage detection and localization, *IEEE Transactions on Instrumentation and Measurement* 71 (2022) 1–13. doi:10.1109/TIM.2022.3144732.
- [21] L. Sun, R. Song, J. Wei, Y. Gao, C. Peng, L. Fan, M. Jiang, L. Zhang, Physics-augmented spatial-temporal graph convolutional network for damage localization using ultrasonic guided waves, *Mechanical Systems and Signal Processing* 221 (2024) 111738. doi:10.1016/j.ymsp.2024.111738.
- [22] M. Rautela, S. Gopalakrishnan, Ultrasonic guided wave based structural damage detection and localization using model assisted convolutional and recurrent neural networks, *Expert Systems with Applications* 167 (2021) 114189. doi:10.1016/j.eswa.2020.114189.
- [23] Y. Song, S. Shan, Y. Zhang, L. Cheng, Physics-guided neural network for structural health monitoring with lamb waves through boundary reflection elimination, *Structural Health Monitoring* 25 (2) (2026) 1219–1236. doi:10.1177/14759217241305050.
- [24] G. Ongie, A. Jalal, C. A. Metzler, R. G. Baraniuk, A. G. Dimakis, R. Willett, Deep learning techniques for inverse problems in imaging, *IEEE Journal on Selected Areas in Information Theory* 1 (1) (2020) 39–56. doi:10.1109/JSAIT.2020.2991563.
- [25] M. Raissi, P. Perdikaris, G. E. Karniadakis, Physics-informed neural networks: A deep learning framework for solving forward and inverse problems involving nonlinear partial differential equations, *Journal of*

- Computational Physics 378 (2019) 686–707. doi:10.1016/j.jcp.2018.10.045.
- [26] E. Del Priore, L. Lampani, Real-time damage detection and localization on aerospace structures using graph neural networks, *Journal of Sensor and Actuator Networks* 14 (5) (2025) 89. doi:10.3390/jsan14050089.
- [27] K. F. Niresi, Z. Zhang, O. Fink, Rins-t: Robust implicit neural solvers for time-series linear inverse problems, *IEEE Transactions on Instrumentation and Measurement* 74 (2025) 1–14.
- [28] O. Fink, V. Sharma, I. Nejjar, L. Von Krannichfeldt, S. Garmaev, Z. Zhang, A. Wei, G. Frusque, F. Forest, M. Zhao, et al., From physics to machine learning and back: Part i-learning with inductive biases in prognostics and health management, *Reliability Engineering & System Safety* (2026) 112213.
- [29] R. Song, L. Sun, Y. Gao, J. Wei, C. Peng, L. Fan, M. Jiang, Unsupervised temperature-compensated damage localization method based on damage to baseline autoencoder and delay-based probabilistic imaging, *Mechanical Systems and Signal Processing* 230 (2025) 112649.
- [30] J. E. Michaels, Detection, localization and characterization of damage in plates with an in situ array of spatially distributed ultrasonic sensors, *Smart Materials and Structures* 17 (3) (2008) 035035. doi:10.1088/0964-1726/17/3/035035.
- [31] Z. Su, L. Ye, Y. Lu, Guided lamb waves for identification of damage in composite structures: A review, *Journal of Sound and Vibration* 295 (3–5) (2006) 753–780. doi:10.1016/j.jsv.2006.01.020.
- [32] J. Moll, J. Kathol, C.-P. Fritzen, M. Moix-Bonet, M. Rennoch, M. Korderdt, A. S. Herrmann, M. G. R. Sause, M. Bach, Open guided waves: online platform for ultrasonic guided wave measurements, *Structural Health Monitoring* 18 (5–6) (2019) 1903–1914. doi:10.1177/1475921718817169.
- [33] Z. Wang, W. Yan, T. Oates, Time series classification from scratch with deep neural networks: A strong baseline, in: 2017 International joint conference on neural networks (IJCNN), IEEE, 2017, pp. 1578–1585.

- [34] S. Hochreiter, Long short-term memory, Neural Computation MIT-Press (1997).
- [35] P. W. Battaglia, J. B. Hamrick, V. Bapst, A. Sanchez-Gonzalez, V. Zambaldi, M. Malinowski, A. Tacchetti, D. Raposo, A. Santoro, R. Faulkner, C. Gulcehre, F. Song, A. Ballard, J. Gilmer, G. E. Dahl, A. Vaswani, K. R. Allen, C. Nash, V. Langston, C. Dyer, N. Heess, D. Wierstra, P. Kohli, M. Botvinick, O. Vinyals, Y. Li, R. Pascanu, Relational inductive biases, deep learning, and graph networks, arXiv preprint arXiv:1806.01261 (2018).